Journal of Medicinal Chemistry

pubs.acs.org/jmc

Article

In Situ Coassembly Induced Mitochondrial Aggregation Activated Drug-Resistant Tumor Treatment

Xian-Yin Dai, Bing Zhang, Qilin Yu,* and Yu Liu*

Cite This: *J. Med. Chem.* 2022, 65, 7363−7370

Read Online

ACCESS | Metrics & More | Article Recommendations | Supporting Information

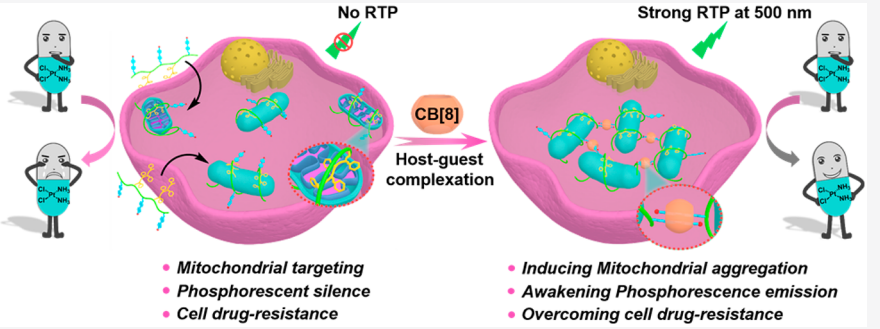

ABSTRACT: Macrocyclic supramolecular coassembly is the current research hotspot for tumor treatment. Herein, we report a multivalent supramolecular coassembly strategy, which not only acquires long-time phosphorescent labeling of mitochondrial aggregation but also strongly enhances chemotherapeutic efficiency against drug-resistant tumors. The mitochondrial aggregation depends on cucurbit[8]uril-mediated cross-linkage of the hyaluronic acid polymer grafted by 4-bromophenylpyridium and mitochondrion-targeting peptide (HABMitP) residing on the mitochondria, taking advantage of the 2:1 homoternary host−guest complexation between cucurbit[8]uril and 4-bromophenylpyridium with an extraordinary binding constant (6.24×10^{12} M^{-2}). In cisplatin-resistant MCF-7 tumor cells, the assembly induced mitochondrial aggregation substantially enhances the antitumor efficiency of cisplatin, with the ratio of apoptotic cells increasing from 43% to 96% compared to treatment with cisplatin alone, and thoroughly inhibits tumor growth *in vivo*. This study provides a novel way for biological phosphorescent imaging and treatment of drug-resistant cancers.

INTRODUCTION

Supramolecular methodology based on molecular recognition of artificially synthetic macrocyclic receptors has evolved as a powerful strategy to modulate the functions of proteins or other biomolecules at both the cell and organelle levels.[1−6] By introduction of binding sites that can be specifically recognized by artificial macrocycles into biomacromolecules or organelles, their corresponding biological functions can be expediently intervened or regulated.[7,8−10] For example, Guo et al. developed a heteromultivalent coassembly consisting of cyclodextrin and calixarene to inhibit the fibrillation of amyloid-β peptides and disaggregate amyloid-β fibrils with reduced amyloid cytotoxicity.[11] Zhou and co-workers utilized cucurbit[7]uril-based host−guest chemistry with adamantane-functionalized 5-formylcytosine to realize a variety of reversible interventions of 5-formylcytosine-targeted biochemical reactions.[12] Moreover, the regulation of mitochondrial aggregation or fusion by supramolecular means is of particular interest and is becoming an increasingly significant research hot spot. Wang et al. reported that the direct artificial supramolecular self-assembly of mitochondria for their aggregation and fusion can contribute to cellular repairs.[13] Ryu and co-workers used mitochondria-targeted thiol-containing monomers that can form fibrous polymeric structures under high intramitochondrial ROS level to induce mitochondrial dysfunction and activate cell necroptosis.[14] We recently reported a supramolecular nanofiber composed of β-cyclodextrin-grafted polysaccharide and targeting peptide-coated magnetic nanoparticles to achieve mitochondrial recruitment and to suppress tumor metastasis both *in vitro* and *in vivo*.[15] These works jointly demonstrate the great potential of supramolecular chemistry in the regulation of biological functions. Notably, among them, cucurbituril plays an important role in mediating the assembly behaviors of biomacromolecules and organelles.

It is well-known that cucurbit[8]uril (CB[8]), as a unique macrocyclic receptor with rigid cavities and stable configuration, has been achieved to fabricate multifarious supra-

Received: March 8, 2022
Published: May 17, 2022

https://doi.org/10.1021/acs.jmedchem.2c00372
J. Med. Chem. 2022, 65, 7363−7370

molecular architectures via host-enhanced intermolecular charge-transfer interactions and has drawn wide attention in biological chemistry and materials science.[16−19] For instance, Isaacs and co-workers designed metal−organic polyhedra decorated with methyl viologen ligands on their external surface as vehicles and achieved delivery of doxorubicin to cancer cells via noncovalent functionalization with a naphthalene-modified prodrug due to the heteroternary charge-transfer formation within CB[8].[20] We also reported the intracellular microtubular aggregation that can be efficiently regulated by using an antimitotic peptide modified with a benzylimidazolium moiety that can be noncovalently encapsulated by CB[8].[21] On the other hand, purely organic room-temperature phosphorescence systems in the aqueous phase have captured growing attention owing to their inherent advantages over fluorescence in bioimaging, such as longer lifetimes and larger Stokes shifts.[22] In particular, phosphorescence can avoid interference from autofluorescence or background fluorescence of cells and tissues.[23−25] The tight encapsulation of CB[8] is proven to be an efficient approach to awaken the phosphorescence of guest molecules by promoting intersystem crossing and inhibiting nonradiative decay.[22,26] Although the regulation of microtubules or mitochondrial aggregation has acquired great progress, mitochondrial aggregation-activated effective resistant tumor treatment and *in situ* long-lived phosphorescence imaging have not been reported to the best of our knowledge and still face grand difficulties at both the supramolecular and biological levels.

In this work, we presented that intracellular mitochondrial aggregation and phosphorescence imaging could be simultaneously realized via an orthogonal supramolecular self-assembly strategy by peptide-mitochondrion recognition, host−guest complexation, and phosphorescence awakening. In our case, hyaluronic acid (HA) was chemically modified with mitochondrion-targeting peptide (MitP) and 4-bromophenylpyridium (BP) together to generate the multivalent supramolecular polymer HABMitP. This polymer specifically targeted the mitochondria via MitP, with 4-bromophenylpyridium residing on the surface of mitochondria. The addition of CB[8] further led to 2:1 homoternary BP+CB[8] complexation, and then exclusively induced supramolecular aggregation of the mitochondria concurrently labeled by awakened phosphorescence (Scheme 1). Significantly, in drug-resistant tumor cells treated with the chemotherapeutic drug cisplatin, the supramolecular assembly deteriorated mitochondrial functions and elicited apoptosis, leading to efficient ablation of drug-resistant tumors. This study provides a multifunctional supramolecular assembly system for efficient phosphorescent labeling of mitochondria and simultaneously inducing mitochondrial aggregation to overcome tumor drug resistance.

RESULTS AND DISCUSSION

Compounds 4-(4-bromophenyl)-1-propylpyridin-1-ium (BrPY-3C) and 1-(2-aminopropyl)-4-(4-bromophenyl)-pyridine-1-ium bromide hydrobromide (BrPY-NH_2) were synthesized according to the routes shown in Schemes S1 and S2 and fully characterized by ^{1}H NMR and ^{13}C NMR spectroscopies (Figures S1−S4). The derived polysaccharide HAB was first synthesized via amide condensation reaction between sodium hyaluronate and BrPY-NH_2 where the substitution degree of 4-(4-bromophenyl)pyridium was calculated as 11.5% by comparing the integral area of proton of 4-(4-bromophenyl)pyridium at 7.82−8.91 ppm with that of

Scheme 1. Representation of the Multivalent Supramolecular Polymer (HABMitP) with CB[8] for Targeted Intracellular Mitochondrial Aggregation

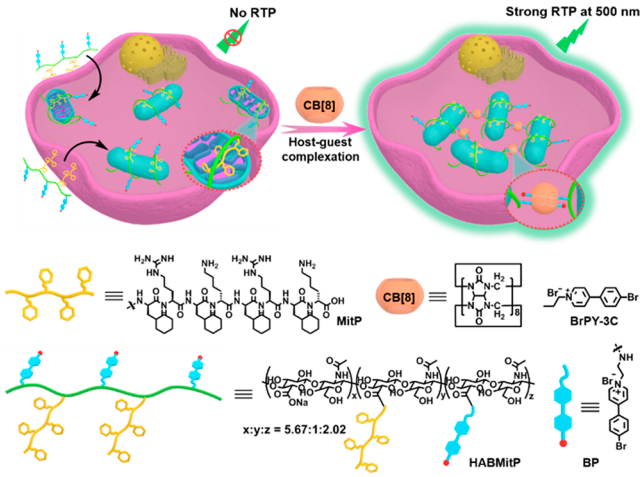

the *N*-acetyl protons of HA at 1.98 ppm (Figure S5). The sequential amide condensation reaction between HAB and MitP-Dde in buffer solution and the deprotection step were conducted to obtain the final multivalent supramolecular polymer HABMitP in which the grafted MitP was determined as 23.6% by comparing the integral area of proton H_c of MitP with that of the *N*-acetyl protons of HA at 1.98 ppm (Figures S6 and S7).

It has been well documented in previous literature that cucurbit[*n*]urils (CB[*n*]s) are able to accommodate phosphorescent guest molecules with positive charge and arouse their phosphorescence intensity in both the solid state and aqueous phase.[27−29] ^{1}H NMR experiments were first performed to investigate the host−guest interaction between a reference compound BrPY-3C and CB[8] (Figure S8). The ^{1}H NMR titration spectra revealed that all of the aromatic proton peaks assigned to protons H_a, H_b, H_c, and H_d of BrPY-3C showed pronounced upfield shifts and peaks assigned to protons H_f and H_g showed downfield shifts upon the gradual addition of CB[8] into the aqueous solution of BrPY-3C, indicating that the 4-(4-bromophenyl)pyridium unit was encapsulated into the cavity of CB[8]. The proton chemical shifts all remained unchanged when the amount of CB[8] was greater than 0.5 equiv which implied a 1:2 host−guest binding stoichiometry between CB[8] and BrPY-3C.

The optical properties of the reference compound BrPY-3C were investigated by UV−vis absorption and photoluminescence emission experiments in aqueous solution. When CB[8] was added to the aqueous solution of BrPY-3C, the absorption maximum at 303 nm gradually decreased with an obvious bathochromic shift, accompanied by the appearance of two isosbestic points at 252 and 323 nm, suggesting the formation of host−guest complex (Figure S9). The association constant (K_s) in BrPY-3C+CB[8] complexation was determined to be 6.24×10^{12} M^{-2} via a nonlinear least-squares curve-fitting method by analyzing the sequential changes in absorbance at 303 nm with varying concentrations of CB[8] (Figure S10). The photoluminescence spectra of free BrPY-3C displayed only an emission peak centered at approximately 390 nm, while a peak at around 500 nm appeared after complexation with CB[8] which was further studied via an oxygen quenching experiment. The emission peak at 500 nm became stronger

https://doi.org/10.1021/acs.jmedchem.2c00372
J. Med. Chem. 2022, 65, 7363−7370

when N_2 was introduced into the BrPY-3C+CB[8] system to exclude the dissolved oxygen in aqueous solution. However, the emission peak at 390 nm showed insensitivity to O_2 with no obvious change in intensity (Figure S11). The photoluminescence intensity of BrPY-3C at 390 nm also followed the same rule in this process. From the gated spectra with the delayed time of 0.2 ms, it was found that only the emission peak at 500 nm still existed along with the disappearance of the peak at 390 nm, indicative of the long-lived emission at 500 nm and short-lived emission at 390 nm, respectively (Figure S12). Meanwhile, the time-resolved decay curves of BrPY-3C +CB[8] at 500 nm were tested under ambient conditions, whose lifetime was determined to be 464.3 μs with a microsecond scale, confirming that the peak at 500 nm was assigned to phosphorescence emission (Figure S13). Moreover, HAB exhibited similar optical properties to BrPY-3C before and after assembly with CB[8]. The absorption peak gradually decreased with a clear bathochromic shift (Figure S14). The peak intensity of HAB+CB[8] at around 500 nm in both photoluminescence spectra and gated spectra (0.2 ms) increased greatly when the solution was bubbled with N_2 to abate the quenching effect of dissolved oxygen on phosphorescence (Figures S15 and S16). The phosphorescence of HAB +CB[8] was much stronger than that of BrPY-3C+CB[8] under the same conditions. Analysis of time-resolved decay data revealed that the phosphorescence lifetime of HAB +CB[8] at 500 nm was 2.20 ms, and that under N_2 was increased to 2.50 ms (Figure S17).

Subsequently, we investigated the photophysical behaviors of the final polymer HABMitP when interacting with CB[8]. The UV−vis absorption spectra and excitation spectra of HABMitP+CB[8] were shown in Figures S18 and S19. The bare HABMitP gave one emission peak centered at 390 nm whose intensity was reduced after adding CB[8] into HABMitP aqueous solution, and the emission peaks here are insensitive to oxygen all the while. However, the intensity of CB[8]-induced emission at 500 nm increased dramatically under N_2 condition (Figure 1A). It could be observed that the emission of bare HABMitP was silent in phosphorescence spectra, whereas the complexation with CB[8] could indeed arouse the phosphorescence emission at 500 nm, proving that both hyaluronic acid skeleton and mitochondrial targeting peptide will not produce any phosphorescence and CB[8] played an important role in inducing and achieving the long-lived phosphorescence of the polymer (Figure 1B). Moreover, the lifetime HABMitP+CB[8] at 390 nm was measured as 693.3 ps, indicative of short-lived fluorescence (Figure 1C). Notably, in contrast with BrPY-3C+CB[8] and HAB+CB[8], HABMitP+CB[8] presented the longest phosphorescence lifetime up to 3.26 ms according to the time-resolved decay curves, which was a relatively longer-lived purely organic room-temperature phosphorescence in aqueous solution, and this value increased to 4.48 ms under oxygen-free condition (Figure 1D). Additionally, bare CB[8] showed no phosphorescence under the same experimental conditions (Figure S20). These results jointly indicated that both CB[8] and polysaccharide-peptide backbone played significant roles for realizing such long-lived phosphorescence of HABMitP. For one thing, the tight encapsulation of the 4-(4-bromophenyl)-pyridium unit by CB[8] with hydrophobic environment can shield quenchers (triplet oxygen and other molecules) from the liquid medium and efficiently enhance the intersystem crossing process to induce the generation of phosphorescence.

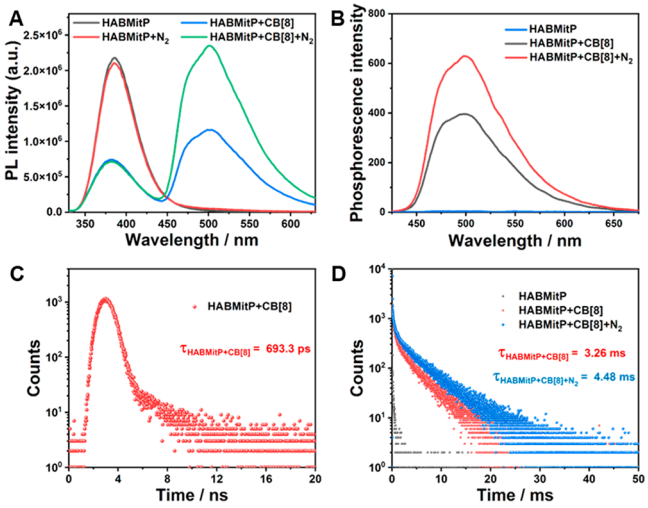

Figure 1. Optical properties of the polymer HABMitP after complexation with CB[8]. (A) Prompt photoluminescence spectra of HABMitP (black), HABMitP/N_2 (red), HABMitP+CB[8] (blue), and HABMitP+CB[8]/N_2 (green) in aqueous solution at 25 °C ([HABMitP] = 5.0 × 10^{-5} M, [CB[8]] = 2.5 × 10^{-5} M). (B) Phosphorescence spectra (delayed by 0.2 ms) of HABMitP (blue), HABMitP+CB[8] (black), and HABMitP+CB[8]/N_2 (red) ([HAB] = 5.0 × 10^{-5} M, [CB[8]] = 2.5 × 10^{-5} M) in aqueous solution at 25 °C (λ_{ex} = 315 nm). (C) Fluorescence decay curves of HABMitP +CB[8] at 380 nm at 298 K. (D) Phosphorescence decay curves of HABMitP (black), HABMitP+CB[8] (red), and HABMitP+CB[8]/N_2 (blue) at 500 nm at 298 K.

For another, the electrostatic interactions and multiple hydrogen bonding originating from the polysaccharide-peptide backbone can also concurrently further restrain molecular motion or rotation and reduce the nonradiative relaxation of the triplet state, thereby greatly improving the phosphorescence performance.

In addition, high-resolution transmission electron microscopy (HR-TEM), dynamic light scattering (DLS), and ζ potential experiments were carried out to fully investigate the topological morphology and surface charge of HABMitP +CB[8]. The TEM images showed that HABMitP alone mainly existed as aggregated nanofibers with lengths of several micrometers, which possibly resulted from aggregation of several linear assemblies at high concentration upon drying during sample preparation (Figure 2A). Surprisingly, in the case of HABMitP+CB[8], homogeneous spherical nanoparticles were clearly observed with an average diameter of 250 nm, which was ascribed to the interpolymer complexation assisted by CB[8] (Figure 2B). Moreover, the ζ potential of the HABMitP was measured to be ∼31.7 mV which is much higher than that of HAB (approximately −14.4 mV) without modification of mitochondrial targeting peptides, suggesting the positively charged surface of such nanofibers HABMitP which was conducive to their accumulation in mitochondria with inherently high negative membrane potential. The tight spherical nanoparticles cross-linking by CB[8] exhibited a further bigger ζ potential of ∼47.5 mV, which ensured that HABMitP could still anchor in mitochondria after assembly with CB[8] (Figure 2C). Furthermore, dynamic light scattering (DLS) showed that the average hydrodynamic diameter of HABMitP+CB[8] was 317.9 nm basically consistent with the TEM result (Figure 2D). These observations demonstrated that CB[8]-mediated multivalent

https://doi.org/10.1021/acs.jmedchem.2c00372
J. Med. Chem. 2022, 65, 7363−7370

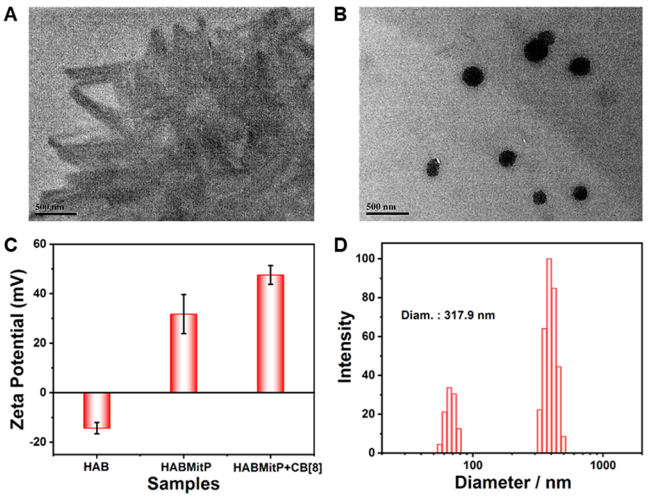

Figure 2. Topological morphology of the polymer HABMitP after complexation with CB[8]. HR-TEM images of (A) individual HABMitP and (B) HABMitP+CB[8]. (C) Surface potential of HAB, HABMitP, and HABMitP+CB[8]. (D) Dynamic light scattering results of HABMitP+CB[8].

supramolecular cross-linking was an essential factor to induce morphological transformation during aggregation of HABMitP through 2:1 BrPY-3C/CB[8] complexation.

The presence of the mitochondrion-targeting peptide on HABMitP motivated us to explore its specific interaction with the mitochondria. Thus, confocal laser scanning microscopic (CLSM) experiments were conducted to explore the subcellular distribution of HABMitP. When the cells were incubated with HABMitP for 12 h and subsequently treated with CB[8] for another 12 h, it could be observed that the green phosphorescence signal of HABMitP+CB[8] appeared and overlapped perfectly with MitoTracker Red (a commercial fluorescent dye for mitochondria staining) accompanied by a high Pearson's correlation coefficient of 0.86 (Figure S21), verifying specific accumulation of the assembly in the mitochondria. Meanwhile, different degrees of mitochondrial aggregation with bright spherically aggregated dots were found (Figure 3A). However, the cells treated with HABMitP alone displayed neither obvious green phosphorescence emission nor mitochondrial aggregation. In another control group, the control cells only stained with MitoTracker Red had the mitochondria distributing evenly in the cytosol with normal regular network-like morphology as indicated by the red fluorescence signal (Figure 3A). Furthermore, TEM observation was employed to directly visualize the mitochondrial morphology in the treated cells. As shown in Figure 3B, the mitochondria of control cells and the cells treated by free HABMitP were uniformly distributed in the cytoplasm. In contrast, the mitochondria of the cells treated by HABMitP and CB[8] exhibited remarkable mitochondrial aggregation behavior. These results suggested that CB[8] not only awakened green phosphorescence signal of HABMitP via the extraordinary host−guest recognition but also led to drastic mitochondrial aggregation due to the CB[8]-mediated cross-linking of HABMitP anchored on mitochondria at the same time.

Owing to the preferential targeting and mitochondrial aggregation capacities of the supramolecular HABMitP +CB[8] assembly, we hypothesized that such aggregation behavior of mitochondria may enhance the treatment performance of antitumor drugs. To verify this, cisplatin (CisPt), a common clinical antitumor chemotherapeutic drug, was used to test the ability of the assembly against drug-resistant tumor cells. After treatment by free CisPt, CisPt+HABMitP, or CisPt +HABMitP+CB[8] for 24 h, the MCF-7/DDP tumor cells, which are resistant to CisPt, were used for assays of mitochondrial functions and cell viability. Confocal microscopy showed that the control cells, together with the cells treated by CisPt or CisPt+HABMitP, had normal network-like mitochondria (Figure 4A). In contrast, the cells treated by CisPt+HABMitP+CB[8] exhibited severely fragmented mitochondria, with the phosphorescence of HAB abundantly overlapping with the fluorescence of MitoTracker (Figure 4A). Quantification of phosphorescence intensity further revealed that the assembly caused much higher phosphorescence intensity than CisPt+HABMitP (Figure 4B), which is consistent with the results of CisPt-free treatments (Figure 3A). These results revealed that the assembly in combination with CisPt strongly disrupted the mitochondrial network, which could be indicated by the phosphorescence of the assembly.

The antitumor activity of CisPt is proven to be associated with ROS accumulation. To further investigate the impact on

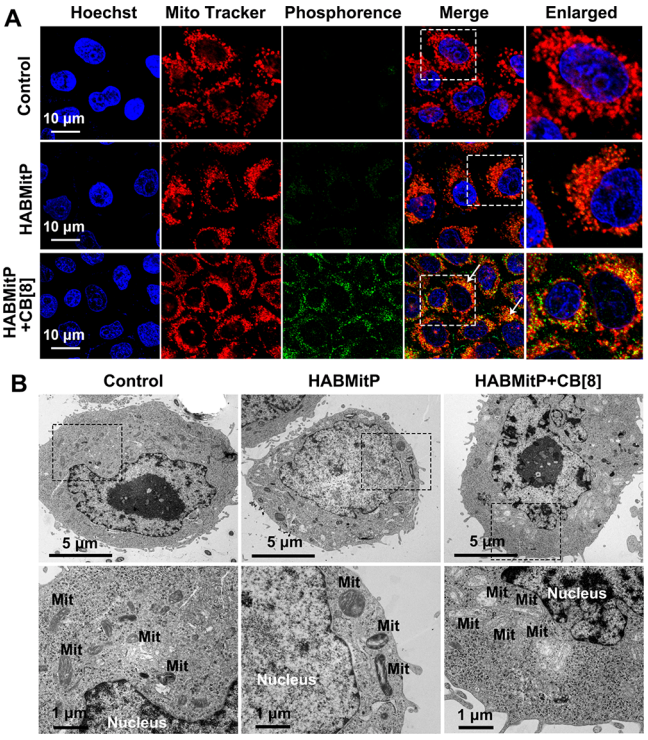

Figure 3. Mitochondrial phosphorescence labeling and aggregation by the HABMitP+CB[8]. (A) Confocal microscopy images of the mitochondria in MCF-7/DDP cells incubated with HABMitP and HABMitP+CB[8] ([HABMitP] = 2.0×10^{-5} M, [CB[8]] = 1.0×10^{-5} M). Hoechst 33342 (blue) was used to stain the nuclei, and MitoTracker (red) was used to stain the mitochondria. The white arrows indicate the aggregated mitochondria labeled by phosphorescence. The regions indicated by white squares are enlarged and shown on the right. (B) TEM images of MCF-7/DDP cells treated with HABMitP and HABMitP+CB[8] ([HABMitP] = 2.0×10^{-5} M, [CB[8]] = 1.0×10^{-5} M). The black arrow indicates representative mitochondrial aggregation induced by HABMitP+CB[8]. The regions indicated by black squares in the first lines are enlarged and shown in the second lines correspondingly.

https://doi.org/10.1021/acs.jmedchem.2c00372
J. Med. Chem. 2022, 65, 7363−7370

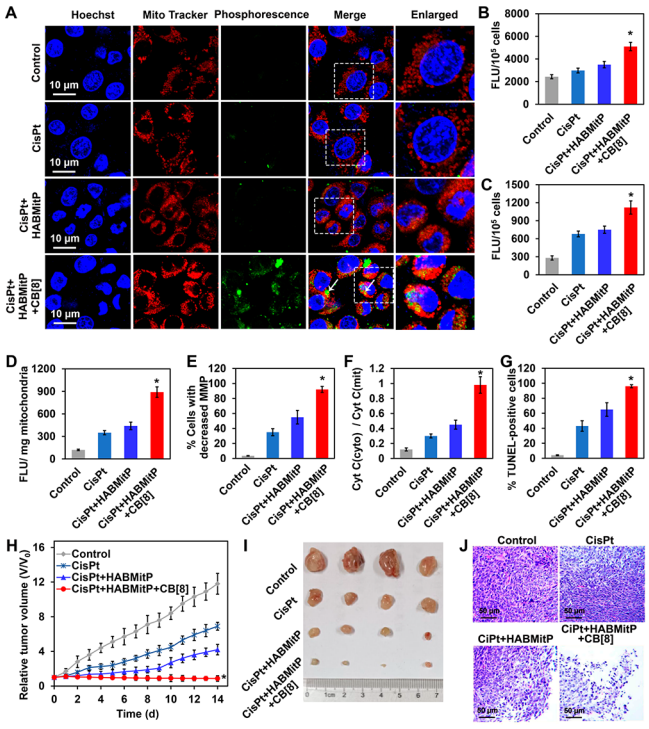

Figure 4. Mitochondrial damage of drug-resistant MCF-7/DDP tumor cells and tumor ablation caused by the CisPt with HAMitP +CB[8]. (A) Confocal microscopy images illustrating mitochondrial morphology in the MCF-7/DDP cells treated by free CisPt ([CisPt] = 1.7 × 10^{-5} M), CisPt+HAMitP ([CisPt] = 1.7 × 10^{-5} M, [HABMitP] = 2.0 × 10^{-5} M) or CisPt+HAMitP+CB[8] ([CisPt] = 1.7 × 10^{-5} M, [HABMitP] = 2.0 × 10^{-5} M, [CB[8]] = 1.0 × 10^{-5} M). The white arrows indicate representative HAB-MitoTracker overlapping sites. The regions indicated by white squares are enlarged and shown on the right. (B) Phosphorescence intensity revealed by ImageJ analysis. (C) Intracellular ROS levels revealed by DCFH-DA staining. (D) Mitochondrial ROS levels revealed by DHE staining. (E) Percent of cells with decreased MMP. (F) Ratio of cytosol cytochrome C (Cyt C(cyto)) to mitochondrial cytochrome C (Cyt C(mit)). (G) Percent of TUNEL-positive (apoptotic) cells. (H) Relative tumor volume of the treated mice burdened with MCF-7/DDP tumors. (I) Tumor photographs of the treated mice. (J) Histological images of the tumors after H&E staining. The asterisks (*) indicate significant difference between the CisPt+HABMitP +CB[8] group and other groups ($P < 0.05$).

mitochondrial functions, intracellular and mitochondrial ROS levels were detected by DCFH-DA staining of whole cells and by dihydroethidium (DHE) staining of isolated mitochondria, respectively. As expected, while free CisPt and CisPt +HABMitP only caused a slight increase in ROS levels, CisPt+HABMitP+CB[8] led to a drastic increase in both intracellular and ROS levels of the tumor cells (Figure 4C,D). The increased mitochondrial ROS accumulation may be attributed to the enhanced mitochondrial targeting of CisPt facilitated by the assembly. Mitochondrial ROS accumulation may further impair mitochondrial membrane potential (MMP), leading to cytochrome C release and apoptosis. Indeed, MMP assays showed that the cells treated by CisPt +HABMitP+CB[8] exhibited severe decrease in MMP, and the percent of cells with decreased MMP reached up to 85% (Figure 4E). In contrast, the cells treated by free CisPt and CisPt+HABMitP only had a low partial of cells with decreased MMP (25−49%, Figure 4E). Consistently, as compared to free CisPt and CisPt+HABMitP, CisPt+HABMitP+CB[8] led to much more severe release of cytochrome C (Cyt C) from the mitochondria to the cytosol (Figure 4F) and caused much higher levels of TdT-mediated dUTP nick-end labeling (TUNEL)-positive (e.g., apoptotic) cells than CisPt and CisPt+HABMitP (96% versus 43% for CisPt and 65% for CisPt+HABMitP, Figure 4G). Consistently, CisPt+HABMitP +CB[8] led to much lower viability in both MCF-7/DDP cells and A549 cells than free CisPt and CisPt+HABMitP (<10% versus >30%, Figure S22). Interestingly, the assembly only slightly impaired viability in noncancerous cells, including the NIH3T3 cells, MRC-5 cells, and 293T cells (Figure S23), which may be attributed to the strong targeting capacity of HABMitP+CB[8] to cancerous cells rather than to non-cancerous cells (Figure S24). This phenomenon is probably derived from the selective recognition between the HA skeleton and HA receptors that are overexpressed on the surface of cancer cells, which can promote the receptor-mediated internalization of HABMitP into the cancer cells, while such process is significantly suppressed in noncancerous cells as a result of lacking HA receptors. These results confirmed that CisPt+HABMitP+CB[8] presented specific targeting ability and strongly impaired the mitochondrial structure and functions, which could further contribute to severe apoptosis in tumor cells and hold great promise to be a safe and promising candidate for drug-resistant tumor treatment.

The *in vivo* antitumor capacity of the assembly was investigated in a mouse model burdening the MCF-7/DDP tumors. First, the *in vivo* distribution of the assembly was evaluated by using Cy5-labeled HABMitP or HABMitP +CB[8]. At 1 h after intravenous injection, both HABMitP and HABMitP+CB[8] were distributed in the whole body, and HABMitP+CB[8] began to accumulate at the tumor site. At 24 h after injection, however, while the fluorescence of HABMitP was remarkably attenuated and only slightly accumulated at the tumor site, the fluorescence intensity of HABMitP+CB[8] remained high at the tumor site (Figure S25). This indicated that HABMitP+CB[8] had prolonged retention time in the mice body and accumulated at the tumor site with much higher levels than HABMitP.

Body weights and tumor volumes were real-time monitored in the mice treated by CisPt-loading HABMitP+CB[8]. All of the mice in different groups had similar body weights during the 14 days after treatment (Figure S26). Meanwhile, histological observation of the main organs revealed that the four groups had intact tissue structures of the organs, i.e., heart, livers, lungs, kidneys, and spleens (Figure S27), indicating good compatibility of the agents. Although all of the agents had no impact on the body weights, CisPt+HABMitP+CB[8] strongly suppressed the growth of tumors, with no obvious increase in the tumor volume (Figure 4H). In contrast, both CisPt and CisPt+HABMitP only partially inhibited tumor growth, with the tumor volumes rapidly growing in the last 5 days (Figure 4H). Tumor imaging further showed that the tumors of the CisPt+HABMitP+CB[8] group were smaller (Figure 4I) and suffered from much more severe tissue damage than that of the other groups (Figure 4J). In addition, as compared to CisPt+HABMitP+CB[8], the CisPt-free HAB-MitP+CB[8] assemblies had lower capacity to disturb the mitochondrial functions (Figure S28A−C) and weakly reduced the tumor weight (Figure S28D), indicating an important role of CisPt in damaging mitochondria and inhibiting tumor

https://doi.org/10.1021/acs.jmedchem.2c00372
J. Med. Chem. 2022, 65, 7363−7370

growth. Therefore, CisPt-loading HABMitP+CB[8] had much stronger inhibitory effect on growth of CisPt-resistant MCF-7/DDP tumors than free CisPt and CisPt+HABMitP. The improvement of CisPt efficiency against the drug-resistant tumors by the HABMitP+CB[8] assembly may be attributed to abnormal accumulation of damaged mitochondria induced by the assembly. The assembly induced mitochondrial aggregation, which compromised the physical interaction between the mitophagic machine and CisPt-damaged mitochondria, inevitably hindered mitophagy for timely eradication of these mitochondria.[30−32] The consequent accumulation of the damaged mitochondira exacerbated release of mitochondrion-derived apoptosis-inducing factors (e.g., cytochrome C) in the cytosol (Figure 4F) and further strongly activated apoptosis of the tumor cells (Figure 4G). These results indicated that supramolecular assembly mediated mitochondrial aggregation is a promising way against drug-resistant tumors.

CONCLUSION

We designed and synthesized a multivalent supramolecular polymer HABMitP simultaneously bearing 4-bromophenylpyridium and mitochondrion-targeting peptide and successfully achieved supramolecular regulation and imaging of mitochondrial behaviors in living cells, benefiting from the mitochondrion-targeted ability of MitP and host−guest interaction of cucurbit[8]uril. Furthermore, such mitochondrial aggregation process can significantly promote deterioration of mitochondrial damage, thus improving the antitumor efficiency toward cisplatin-resistant MCF-7 cells and tumors both *in vitro* and *in vivo*. This work presents a convenient and feasible supramolecular approach for regulating and labeling mitochondrial behaviors and holds great promise for combating drug-resistant cancer.

EXPERIMENTAL SECTION

Materials. All the chemicals used in the present work were purchased from Sigma-Aldrich and directly used without further purifcation unless otherwise noted. MitP-Dde (Fx-r-Fx-K(Dde)-Fx-r-Fx-K(Dde)) was synthesized by means of the solid phase method according to the previous report.[15] 4-(4-Bromophenyl)pyridine was obtained from 1-bromo-4-iodobenzene and pyridine-4-boronic acid via Suzuki coupling reaction.[33] All compounds are >95% pure by HPLC analysis or ^{1}H NMR/^{13}C NMR spectroscopy.

Instruments. NMR spectra were acquired via a Bruker AV400 instrument. A Shimadzu UV-3600 spectrophotometer with a PTC-348WI temperature controller in a quartz cell (light path 10 mm) was utilized to record UV−vis absorption spectra at 298 K. Photoluminescence spectra and lifetimes were obtained on an FLS980 instrument (Edinburg Instruments, Livingstone, U.K.). Phosphorescence emission spectra (delay 0.2 ms) were recorded in a conventional quartz cell (10 × 10 × 45 mm) on a Varian Cary Eclipse at 298 K. The morphologies were observed by transmission electron microscope (FEI Tecnai G^2 F20 microscope operating at 200 kV). The size distribution was measured by a laser light scattering spectrometer (BI-200SM) equipped with a digital correlator (Turbo Corr) at 636 nm at a scattering angle of 90°. ζ potential analysis was performed on a Brookhaven ZetaPALS (Brookhaven Instrument, USA) at 298 K. CCK8 assay results were detected by a microplate reader (American BioTek Synergy 4). The confocal images were obtained by a confocal microscope (FV1000, Olympus, Japan).

Synthesis of BrPy-NH$_2$. 4-(4-Bromophenyl)pyridine (470 mg, 2.00 mmol) was first dissolved in 20 mL of anhydrous dimethylformamide, and 2-bromoethylamine hydrobromide (615 mg, 3.00 mmol) was added to the above mixture to obtain a clear solution under strong agitation. Then the solution was heated to 90 °C for 24 h. The reaction mixture was allowed to cool to room temperature during which time a large amount of precipitate formed and then filtered, and the obtained solid was sufficiently washed with diethyl ether to afford BrPy-NH$_2$ as an off-white solid (456 mg, yield 52%). ^{1}H NMR (400 MHz, DMSO-d_6, ppm) δ 9.19 (d, J = 6.8 Hz, 2H), 8.66 (d, J = 6.8 Hz, 2H), 8.25 (s, 2H), 8.10 (d, J = 8.6 Hz, 2H), 7.89 (d, J = 8.5 Hz, 2H), 4.95 (t, J = 5.5 Hz, 2H), 3.60 (t, J = 5.6 Hz, 2H). ^{13}C NMR (100 MHz, DMSO-d_6, ppm) δ 154.54 (s), 146.09 (s), 133.23 (s), 133.09 (s), 130.64 (s), 126.91 (s), 125.01 (s), 57.44 (s), 39.48 (s).

Synthesis of BrPy-3C. 4-(4-Bromophenyl)pyridine (470 mg, 2.00 mmol) was first dissolved in 15 mL of anhydrous acetonitrile under stirring conditions, and 1-bromopropane (1 mL) was added to the above mixture to obtain a clear solution. Then the solution was heated to 90 °C for 12 h. The reaction mixture was allowed to cool to room temperature and excess solvent was removed by rotary evaporation. The obtained solid was fully washed with diethyl ether to afford BrPy-3C as an off-white solid (493 mg, yield 69%). ^{1}H NMR (400 MHz, DMSO-d_6, ppm) δ 9.20 (d, J = 6.2 Hz, 2H), 8.59 (t, J = 18.3 Hz, 2H), 8.06 (d, J = 8.3 Hz, 2H), 7.82 (t, J = 17.2 Hz, 2H), 4.60 (t, J = 7.0 Hz, 2H), 2.24−1.67 (q, 2H), 0.90 (t, J = 7.2 Hz, 3H). ^{13}C NMR (100 MHz, DMSO-d_6, ppm) δ 153.43 (s), 144.89 (s), 132.74 (s), 132.60 (s), 130.17 (s), 126.15 (s), 124.49 (s), 61.18 (s), 24.11 (s), 10.23 (s).

Synthesis of HAB. Sodium hyaluronate (M_w = 200 000) (250 mg, 1.25 μmol) was added into 150 mL of freshly prepared PBS (0.1 M, pH 7.2), and the reactive material was stirred vigorously for 30 min to dissolve completely at room temperature. After that, 1-ethyl-3-(3-dimethylaminopropyl)carbodiimide hydrochloride (EDCl) (419 mg, 2.2 mmol) and *N*-hydroxysuccinimide (NHS) (253 mg, 2.2 mmol) were successively added to guarantee complete dissolution. Subsequently, BrPy-NH$_2$ (549 mg, 1.25 mmol) in 50 mL of PBS was added to the above solution, and the mixture was stirred at room temperature for 24 h. Last, the resultant solution was dialyzed against an excess amount of pure water for 7 days. The targeted product HAB was afforded as a white fluffy powder (102 mg, yield 23%) after freeze-drying. The content of BrPy-NH$_2$ in the conjugate was measured by the ^{1}H NMR integral of the corresponding characteristic peak of the benzene ring and the HA backbone.

Synthesis of HABMitP. An amount of 50 mg of HAB was dissolved in 25 mL of MES buffer (50 mM, pH = 6.0), and then 20 mg of EDCl and 22 mg of NHSS were added into the solution. After the mixture was stirred for 30 min, 10 mg of MitP-Dde was added into the reaction system. The mixture was stirred at 4 °C for another 12 h and then dialyzed against an excess amount of pure water for 2 days to remove unreacted raw materials and salts. The remaining solution was concentrated to 10 mL, and another 10 mL of ethanol was added. Subsequently, 200 μL of hydrazine monhydrate was added to remove the protective group of MitP at room temperature for 12 h. The pure HABMitP powder (28 mg, yield 47%) was obtained by freeze-drying followed by an extra 5 days of dialysis and was characterized by ^{1}H NMR.

Cell Experiments. The cancerous MCF-7/DDP (CisPt-resistant) and A549 cells were purchased from LMAI, China. The noncancerous NIH3T3, MRC-5, and 293T cells were purchased from the Cell Resource Center, Chinese Academy of Medical Science, China. To investigate the effect of the free cisplatin (CisPt), CisPt+HAMMitP, and CisPt+HAMMitP+CB[8] on the viability of each cell line, the cells were first cultured in 96-well microplates with corresponding culture media for 24 h, and then free CisPt ([CisPt] = 1.7 × 10^{-5} M), CisPt+HAMitP ([CisPt] = 1.7 × 10^{-5} M, [HABMitP] = 2.0 × 10^{-5} M), or CisPt+HAMitP+CB[8] ([CisPt] = 1.7 × 10^{-5} M, [HABMitP] = 2.0 × 10^{-5} M, [CB[8]] = 1.0 × 10^{-5} M) was added into the cell cultures (12 h of HAMitP or CisPt+HAMitP treatment, followed by another 12 h of CB[8] treatment). After 24 h of further culturing, the cells were used for CCK-8 assay kits. To evaluate uptake of HAMitP+CB[8] by the tested cells, the cells were treated by HAMitP for 12 h ([HABMitP] = 2.0 × 10^{-5} M) and treated by CB[8] ([CB[8]] = 1.0 × 10^{-5} M) for a further 12 h. The cells were then washed twice by PBS. The cells were then used for measurement of fluorescence

https://doi.org/10.1021/acs.jmedchem.2c00372
J. Med. Chem. 2022, 65, 7363−7370

intensity. To measure cellular apoptosis induced by the assembly, the treated cells were stained by one step TUNEL apoptosis assay kit (red fluorescence, Beyotime, China) and then analyzed by flow cytometry (FACSCalibur, BD Biosciences).

To observe mitochondrial morphology of the MCF-7/DDP cells, the cells were cultured in confocal dishes for 24 h and then treated by HAMitP, HAMitP+CB[8] (12 h of HAMitP treatment, followed by another 12 h of CB[8] treatment), CisPt+HAMitP, or CisPt +HAMitP+CB[8] (12 h of CisPt+HAMitP treatment, followed by another 12 h of CB[8] treatment) for a further 24 h. The cells were then washed twice by PBS and stained by Hoechst 33342 (5 mg/L, Sigma, USA) and MitoTracker Red (100 nM, Beyotime, China) for 30 min. The cells were then observed by confocal microscopy (A1+, Nikon, Japan). The cells were also digested by trypsin and fixed by glutaric dialdehyde for ultrathin sectioning and TEM observation.

To investigate the impact of the assembly on mitochondrial membrane potential (MMP), the treated cells were harvested and stained by JC-1 (50 mg/L, Sigma, USA) for 30 min. Fluorescence intensity of JC-1 aggreates (red fluoresence) and monomers (green fluorescence) cells was then detected by flow cytometry (FACSCalibur, BD Biosciences). To detect mitochondrial cytochrome C release mitochondrial ROS levels, the mitochondria were isolated by predisrupting the treated cells by homolyzers, followed by centrifugation at 12 000 rpm to pellet the mitochondria. Mitochondrial cytochrome C and cytosol cytochrome C were detected by Western blotting using cytochrome C monoantibody (Abcam, USA) and quantified by ImageJ software. Mitochondrial ROS levels were detected by dihydroethidium (DHE) staining and fluorescence microplate readers.

Animal Experiments. The animal experiments were approved by the Animal Care and Use Committee at Nankai University (accreditation number 2021-SYDWLL-000023). An MCF-7/DDP tumor-burdened mouse model was used to evaluate the *in vivo* antitumor capacity of the assembly. First, the 4-week-old female BALB/c nude mice were subcutaneously inoculated with 200 μL of MCF-7/DDP tumor cells (1.0×10^8 cells/mL) per mouse. After 5 days of feeding, a 1 mL solution of CisPt ([CisPt] = 1.7×10^{-5} M), CisPt+HAMitP ([CisPt] = 1.7×10^{-5} M, [HABMitP] = 2.0×10^{-5} M), or CisPt+HAMitP+CB[8] ([CisPt] = 1.7×10^{-5} M, [HABMitP] = 2.0×10^{-5} M, [CB[8]] = 1.0×10^{-5} M) was intravenously injected at tail veils per mouse per day for 3 days. Tumor volumes and body weights were monitored from the first day of treatment to the 14th day. The tumor tissues, together with the main organs, including hearts, livers, lungs, kidneys, and spleens, were sampled from the treated mice and fixed by 4% formaldehyde for sectioning and histopathological observation by H&E staining. To observe *in vivo* distribution of the polymer and assembly, a 1 mL solution of Cy5-labeled HAMitP ([HABMitP] = 2.0×10^{-5} M) or HAMitP+CB[8] ([HABMitP] = 2.0×10^{-5} M, [CB[8]] = 1.0×10^{-5} M) was injected into the tumor-burdened mice. The Cy5 fluorescence in the mice was then monitored by an *in vivo* animal imaging system (IVIS Lumina II, Xenogen, USA).

Statistical Analysis. Each experiment was performed in triplicate. The results were shown with the mean and standard derivates. Differences between the groups were evaluated by one-way analysis of variance (ANOVA) test ($P < 0.05$) using the SPSS software.

■ ASSOCIATED CONTENT

Supporting Information

The Supporting Information is available free of charge at https://pubs.acs.org/doi/10.1021/acs.jmedchem.2c00372.

Details of relevant syntheses, compound characterization data, additional UV−vis absorption spectra, prompt photoluminescence spectra, phosphorescence emission spectra, and cell viability (PDF)

■ AUTHOR INFORMATION

Corresponding Authors

Qilin Yu − *Key Laboratory of Molecular Microbiology and Technology, College of Life Sciences, Nankai University, Tianjin 300071, P. R. China;* orcid.org/0000-0003-0473-5111; Email: yuqilin@mail.nankai.edu.cn

Yu Liu − *College of Chemistry, State Key Laboratory of Elemento-Organic Chemistry, Nankai University, Tianjin 300071, P. R. China;* orcid.org/0000-0001-8723-1896; Email: yuliu@nankai.edu.cn

Authors

Xian-Yin Dai − *College of Chemistry, State Key Laboratory of Elemento-Organic Chemistry, Nankai University, Tianjin 300071, P. R. China*

Bing Zhang − *College of Chemistry, State Key Laboratory of Elemento-Organic Chemistry, Nankai University, Tianjin 300071, P. R. China*

Complete contact information is available at: https://pubs.acs.org/10.1021/acs.jmedchem.2c00372

Notes

The authors declare no competing financial interest.

■ ACKNOWLEDGMENTS

This work was financially supported by the National Natural Science Foundation of China (Grant 22131008).

■ ABBREVIATIONS USED

BP, 4-bromophenylpyridium; BrPY-3C, 4-(4-bromophenyl)-1-propylpyridin-1-ium; BrPY-NH_2, 1-(2-aminopropyl)-4-(4-bromophenyl)pyridine-1-ium bromide hydrobromide; CB[8], cucurbit[8]uril; HA, hyaluronic acid; HABMitP, hyaluronic acid polymer grafted by 4-bromophenylpyridium and mitochondrion-targeting peptide; MitP, mitochondrion-targeting peptide

■ REFERENCES

(1) Yu, G.; Ma, Y.; Han, C.; Yao, Y.; Tang, G.; Mao, Z.; Gao, C.; Huang, F. A Sugar-Functionalized Amphiphilic Pillar[5]arene: Synthesis, Self-Assembly in Water, and Application in Bacterial Cell Agglutination. *J. Am. Chem. Soc.* **2013**, *135* (28), 10310−10313.

(2) Wang, Y.; Zhang, X.; Zou, G.; Peng, S.; Liu, C.; Zhou, X. Detection and Application of 5-Formylcytosine and 5-Formyluracil in DNA. *Acc. Chem. Res.* **2019**, *52* (4), 1016−1024.

(3) Rennie, M. L.; Fox, G. C.; Pérez, J.; Crowley, P. B. Autoregulated Protein Assembly on a Supramolecular Scaffold. *Angew. Chem., Int. Ed.* **2018**, *57* (42), 13764−13769.

(4) Luo, Q.; Hou, C.; Bai, Y.; Wang, R.; Liu, J. Protein Assembly: Versatile Approaches to Construct Highly Ordered Nanostructures. *Chem. Rev.* **2016**, *116* (22), 13571−13632.

(5) Liu, Y. H.; Zhang, Y. M.; Yu, H. J.; Liu, Y. Cucurbituril-Based Biomacromolecular Assemblies. *Angew. Chem., Int. Ed.* **2021**, *60* (8), 3870−3880.

(6) Zhang, Y. M.; Xu, X.; Yu, Q.; Liu, Y. H.; Zhang, Y. H.; Chen, L. X.; Liu, Y. Reversing the Cytotoxicity of Bile Acids by Supramolecular Encapsulation. *J. Med. Chem.* **2017**, *60* (8), 3266−3274.

(7) McGovern, R. E.; Fernandes, H.; Khan, A. R.; Power, N. P.; Crowley, P. B. Protein Camouflage in Cytochrome c−Calixarene Complexes. *Nat. Chem.* **2012**, *4* (7), 527−533.

(8) Bosmans, R. P. G.; Briels, J. M.; Milroy, L.-G.; de Greef, T. F. A.; Merkx, M.; Brunsveld, L. Supramolecular Control over Split-Luciferase Complementation. *Angew. Chem., Int. Ed.* **2016**, *55* (31), 8899−8903.

(9) Cao, W.; Qin, X.; Wang, Y.; Dai, Z.; Dai, X.; Wang, H.; Xuan, W.; Zhang, Y.; Liu, Y.; Liu, T. A General Supramolecular Approach to Regulate Protein Functions by Cucurbit[7]uril and Unnatural Amino Acid Recognition. *Angew. Chem., Int. Ed.* **2021**, *60* (20), 11196−11200.
(10) de Vink, P. J.; Briels, J. M.; Schrader, T.; Milroy, L.-G.; Brunsveld, L.; Ottmann, C. A Binary Bivalent Supramolecular Assembly Platform Based on Cucurbit[8]uril and Dimeric Adapter Protein 14−3-3. *Angew. Chem., Int. Ed.* **2017**, *56* (31), 8998−9002.
(11) Xu, Z.; Jia, S.; Wang, W.; Yuan, Z.; Jan Ravoo, B.; Guo, D.-S. Heteromultivalent Peptide Recognition by Co-assembly of Cyclodextrin and Calixarene Amphiphiles Enables Inhibition of Amyloid Fibrillation. *Nat. Chem.* **2019**, *11* (1), 86−93.
(12) Wang, S.-R.; Song, Y.-Y.; Wei, L.; Liu, C.-X.; Fu, B.-S.; Wang, J.-Q.; Yang, X.-R.; Liu, Y.-N.; Liu, S.-M.; Tian, T.; Zhou, X. Cucurbit[7]uril-Driven Host−Guest Chemistry for Reversible Intervention of 5-Formylcytosine-Targeted Biochemical Reactions. *J. Am. Chem. Soc.* **2017**, *139* (46), 16903−16912.
(13) Sun, C.; Wang, Z.; Yue, L.; Huang, Q.; Cheng, Q.; Wang, R. Supramolecular Induction of Mitochondrial Aggregation and Fusion. *J. Am. Chem. Soc.* **2020**, *142* (39), 16523−16527.
(14) Kim, S.; Jana, B.; Go, E. M.; Lee, J. E.; Jin, S.; An, E.-K.; Hwang, J.; Sim, Y.; Son, S.; Kim, D.; Kim, C.; Jin, J.-O.; Kwak, S. K.; Ryu, J.-H. Intramitochondrial Disulfide Polymerization Controls Cancer Cell Fate. *ACS Nano* **2021**, *15* (9), 14492−14508.
(15) Yu, Q.; Zhang, Y.-M.; Liu, Y.-H.; Xu, X.; Liu, Y. Magnetism and Photo Dual-Controlled Supramolecular Assembly for Suppression of Tumor Invasion and Metastasis. *Sci. Adv.* **2018**, *4*, No. eaat2297.
(16) Yang, B.; Yu, S.-B.; Zhang, P.-Q.; Wang, Z.-K.; Qi, Q.-Y.; Wang, X.-Q.; Xu, X.-H.; Yang, H.-B.; Wu, Z.-Q.; Liu, Y.; Ma, D.; Li, Z.-T. Self-Assembly of a Bilayer 2D Supramolecular Organic Framework in Water. *Angew. Chem., Int. Ed.* **2021**, *60* (50), 26268−26275.
(17) Pazos, E.; Novo, P.; Peinador, C.; Kaifer, A. E.; García, M. D. Cucurbit[8]uril (CB[8])-Based Supramolecular Switches. *Angew. Chem., Int. Ed.* **2019**, *58* (2), 403−416.
(18) Hou, C.; Li, J.; Zhao, L.; Zhang, W.; Luo, Q.; Dong, Z.; Xu, J.; Liu, J. Construction of Protein Nanowires through Cucurbit[8]uril-based Highly Specific Host-Guest Interactions: An Approach to the Assembly of Functional Proteins. *Angew. Chem., Int. Ed.* **2013**, *52* (21), 5590−5593.
(19) Li, Y.; Li, Q.; Miao, X.; Qin, C.; Chu, D.; Cao, L. Adaptive Chirality of an Achiral Cucurbit[8]uril-Based Supramolecular Organic Framework for Chirality Induction in Water. *Angew. Chem., Int. Ed.* **2021**, *60* (12), 6744−6751.
(20) Samanta, S. K.; Moncelet, D.; Briken, V.; Isaacs, L. Metal−Organic Polyhedron Capped with Cucurbit[8]uril Delivers Doxorubicin to Cancer Cells. *J. Am. Chem. Soc.* **2016**, *138* (43), 14488−14496.
(21) Zhang, Y. M.; Liu, J. H.; Yu, Q.; Wen, X.; Liu, Y. Targeted Polypeptide−Microtubule Aggregation with Cucurbit[8]uril for Enhanced Cell Apoptosis. *Angew. Chem., Int. Ed.* **2019**, *58* (31), 10553−10557.
(22) Yu, H.-J.; Zhou, Q.; Dai, X.; Shen, F.-F.; Zhang, Y.-M.; Xu, X.; Liu, Y. Photooxidation-Driven Purely Organic Room-Temperature Phosphorescent Lysosome-Targeted Imaging. *J. Am. Chem. Soc.* **2021**, *143* (34), 13887−13894.
(23) Ma, X.-K.; Liu, Y. Supramolecular Purely Organic Room-Temperature Phosphorescence. *Acc. Chem. Res.* **2021**, *54* (17), 3403−3414.
(24) Zhang, T.; Ma, X.; Wu, H.; Zhu, L.; Zhao, Y.; Tian, H. Molecular Engineering for Metal-Free Amorphous Materials with Room-Temperature Phosphorescence. *Angew. Chem., Int. Ed.* **2020**, *59* (28), 11206−11216.
(25) Ma, X.; Wang, J.; Tian, H. Assembling-Induced Emission: An Efficient Approach for Amorphous Metal-Free Organic Emitting Materials with Room-Temperature Phosphorescence. *Acc. Chem. Res.* **2019**, *52* (3), 738−748.
(26) Zhou, W.-L.; Lin, W.; Chen, Y.; Dai, X.-Y.; Liu, Z.-X.; Liu, Y. Multivalent Supramolecular Assembly with Ultralong Organic Room Temperature Phosphorescence, High Transfer Efficiency and Ultrahigh Antenna Effect in Water. *Chem. Sci.* **2022**, *13*, 573−579.
(27) Wang, J.; Huang, Z.; Ma, X.; Tian, H. Visible-Light-Excited Room-Temperature Phosphorescence in Water by Cucurbit[8]uril-Mediated Supramolecular Assembly. *Angew. Chem., Int. Ed.* **2020**, *59* (25), 9928−9933.
(28) Huo, M.; Dai, X. Y.; Liu, Y. Uncommon Supramolecular Phosphorescence-Capturing Assembly Based on Cucurbit[8]uril-Mediated Molecular Folding for Near-Infrared Lysosome Imaging. *Small* **2022**, *18* (1), 2104514.
(29) Garain, S.; Garain, B. C.; Eswaramoorthy, M.; Pati, S. K.; George, S. J. Light-Harvesting Supramolecular Phosphors: Highly Efficient Room Temperature Phosphorescence in Solution and Hydrogels. *Angew. Chem., Int. Ed.* **2021**, *60* (36), 19720−19724.
(30) Suomalainen, A.; Battersby, B. J. Mitochondrial Diseases: the Contribution of Organelle Stress Responses to Pathology. *Nat. Rev. Mol. Cell Biol.* **2018**, *19* (2), 77−92.
(31) Poole, L. P.; Macleod, K. F. Mitophagy in Tumorigenesis and Metastasis. *Cell. Mol. Life Sci.* **2021**, *78* (8), 3817−3851.
(32) Xie, C.; Zhuang, X.-X.; Niu, Z.; Ai, R.; Lautrup, S.; Zheng, S.; Jiang, Y.; Han, R.; Gupta, T. S.; Cao, S.; Lagartos-Donate, M. J.; Cai, C.-Z.; Xie, L.-M.; Caponio, D.; Wang, W.-W.; Schmauck-Medina, T.; Zhang, J.; Wang, H.-l.; Lou, G.; Xiao, X.; Zheng, W.; Palikaras, K.; Yang, G.; Caldwell, K. A.; Caldwell, G. A.; Shen, H.-M.; Nilsen, H.; Lu, J.-H.; Fang, E. F. Amelioration of Alzheimer's Disease Pathology by Mitophagy Inducers Identified via Machine Learning and a Cross-Species Workflow. *Nat. Biomed. Eng.* **2022**, *6* (1), 76−93.
(33) Su, S.-J.; Tanaka, D.; Li, Y.-J.; Sasabe, H.; Takeda, T.; Kido, J. Novel Four-Pyridylbenzene-Armed Biphenyls as Electron-Transport Materials for Phosphorescent OLEDs. *Org. Lett.* **2008**, *10* (5), 941−944.

https://doi.org/10.1021/acs.jmedchem.2c00372
J. Med. Chem. 2022, 65, 7363−7370